Contents lists available at ScienceDirect

Icarus

Bright carbonate surfaces on Ceres as remnants of salt-rich water fountains

O. Ruesch[a,b,*], L.C. Quick[c], M.E. Landis[d], M.M. Sori[d], O. Čadek[e], P. Brož[f], K.A. Otto[g], M.T. Bland[h], S. Byrne[d], J.C. Castillo-Rogez[i], H. Hiesinger[j], R. Jaumann[g], K. Krohn[g], L.A. McFadden[k], A. Nathues[l], A. Neesemann[m], F. Preusker[g], T. Roatsch[g], P.M. Schenk[n], J.E.C. Scully[i], M.V. Sykes[o], D.A. Williams[p], C.A. Raymond[i], C.T. Russell[q]

[a] NASA Goddard Space Flight Center/USRA, Greenbelt, MD 20771, USA
[b] ESTEC, European Space Agency, Keplerlaan 1, 2201 AZ Noordwijk, The Netherlands
[c] Smithsonian Institution, National Air and Space Museum, Center for Earth and Planetary Studies (CEPS), Washington, DC 20560, USA
[d] Lunar and Planetary Laboratory, University of Arizona, Tucson, AZ 85721, USA
[e] Department of Geophysics, Faculty of Mathematics and Physics, Charles University, 180 00 Prague, Czech Republic
[f] Institute of Geophysics of the Czech Academy of Science, 141 31 Prague, Czech Republic
[g] Deutsches Zentrum für Luft- und Raumfahrt (DLR), 12489 Berlin, Germany
[h] U. S. Geological Survey, Flagstaff, AZ 86001, USA
[i] Jet Propulsion Laboratory, Caltech, Pasadena, CA 91125, USA
[j] Institut für Planetologie, Westfälische Wilhelms-Universität, 48149 Münster, Germany
[k] NASA Goddard Space Flight Center, Greenbelt, MD 20771, USA
[l] Max-Planck-Institut für Sonnensystemforschung (MPS), 37007 Göttingen, Germany
[m] Institute of Geological Sciences, Freie Universität Berlin, 12249 Berlin, Germany
[n] Lunar and Planetary Institute, Houston, TX 77058, USA
[o] Planetary Science Institute, Tucson, AZ 85719, USA
[p] School of Earth & Space Exploration, Arizona State University, Tempe, AZ 85004, USA
[q] Earth, Planetary and Space Sciences, UCLA, Los Angeles, CA 90095, USA

ARTICLE INFO

ABSTRACT

Vinalia and Cerealia Faculae are bright and salt-rich localized areas in Occator crater on Ceres. The predominance of the near-infrared signature of sodium carbonate on these surfaces suggests their original material was a brine. Here we analyze Dawn Framing Camera's images and characterize the surfaces as composed of a central structure, either a possible depression (Vinalia) or a central dome (Cerealia), and a discontinuous mantling. We consider three materials enabling the ascent and formation of the faculae: ice ascent with sublimation and carbonate particle lofting, pure gas emission entraining carbonate particles, and brine extrusion. We find that a mechanism explaining the entire range of morphologies, topographies, as well as the common composition of the deposits is brine fountaining. This process consists of briny liquid extrusion, followed by flash freezing of carbonate and ice particles, particle fallback, and sublimation. Subsequent increase in briny liquid viscosity leads to doming. Dawn observations did not detect currently active water plumes, indicating the frequency of such extrusions is longer than years.

© 2018 Elsevier Inc. All rights reserved.

1. Introduction

The surface of Ceres records a history of internal activity that originates from rock-water interactions. Remarkable features of these interactions are bright spots (*faculae*) (Nathues et al., 2015; De Sanctis et al., 2016), such as Vinalia and Cerealia Faculae, the largest and brightest occurrences, located within Occator impact crater (Fig. 1, 20°N, 240°E). Near-infrared observations of these bright spots identified anhydrous sodium carbonate (Na_2CO_3) as the dominant component, mixed with minor phyllosilicates and opaques minerals (i.e., spectrally bland with low albedo), a mineralogy also detected at the cryovolcanic dome Ahuna Mons (Ruesch et al., 2016; Zambon et al., 2017). On a compositional basis, the involvement of subsurface brine at the faculae has been proposed

* Corresponding author at: Planetary Systems Laboratory – code 693, NASA Goddard Space Flight Center, 8800 Greenbelt Road, Greenbelt, MD 20771, USA.
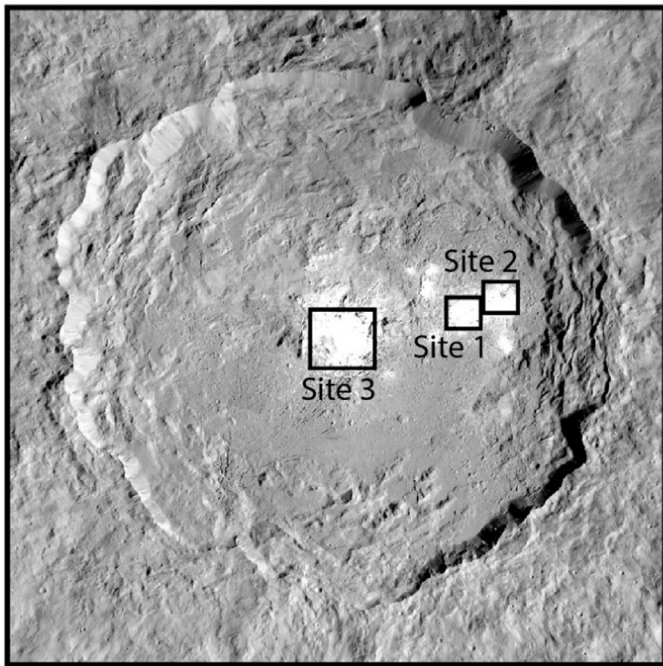E-mail address: ruesch@protonmail.com (O. Ruesch).

Fig. 1. FC mosaic of the Occator impact crater (92-km in diameter) on Ceres hosting bright carbonate bearing surfaces named Vinalia Faculae (Sites 1 and 2) and Cerealia Facula (Site 3). Insets indicate location of Figs. 2 and 3.

(De Sanctis et al., 2016). The brine consists of liquid water with an abundance of dissolved salts, mostly carbonates, gases and entrained altered solids (De Sanctis et al., 2016; Zolotov, 2017; Vu et al., 2017). However, determining how the faculae formed and at which stage of the emplacement the water was present are key questions that need to be addressed. Determining faculae emplacement conditions has direct consequences for Ceres' thermal and geochemical evolution, as well as for faculae composition. The possibility of water reaching the surface is of importance for the currently debated results related to the existence of present-day water sublimation (Nathues et al., 2015; Thangjam et al., 2016; Schroeder et al., 2017) and proposed past cryovolcanism (Krohn et al., 2016; Nathues et al., 2018).

Three means of transport are conceivable to bring subsurface carbonate-rich material to the surface: (i) ice ascent, (ii) gas emission from clathrate decomposition, (iii) brine eruption (hereafter transporting materials). (i) Water ice abundance up to 30–40 vol%, on average, in Ceres' crust is permitted from crater relaxation models (Bland et al., 2016), and confirmed to be present by detections of localized ice exposures (Combe et al., 2016; Nathues et al., 2017a), and regolith ice at latitudes above 40° (Prettyman et al., 2017). In the ice ascent scenario, carbonate-bearing ice reaches the surface driven by buoyancy (Ceres' outer crust has a density of 1287 kg m^{-3} (Ermakov et al., 2017)). Once at the surface, sublimating ice would leave behind a carbonate salt lag deposit and would loft salt particles (e.g., Thomas et al., 2015). (ii) Evidence for clathrate within Ceres is circumstantial, based on thermal-physical-chemical modeling of Ceres evolution (Castillo-Rogez and McCord, 2010; Castillo-Rogez et al., submitted) and on crustal properties inferred from topography (Bland et al., 2016; Fu et al., 2017). In this scenario, fractures caused by Occator impact lead to decompression in a (methane) clathrate reservoir, with subsequent clathrate decomposition and gas release (e.g., Kieffer et al., 2006). Local concentration of carbonate particles, already present in the crust are entrained by the venting gas up to the surface and deposited back by fallback. In these two first scenarios, the crystallization of carbonate particles, as studied for example in Vu et al. (2017) and

Zolotov (2017), occurred well before the emplacement of the faculae. (iii) In the third scenario, liquid brine reaches the surface through a fractured subsurface driven by buoyancy and decompression with gas exsolution, as suggested for cryovolcanic flow landforms (Neveu and Desh, 2015; Krohn et al., 2016). Once exposed to vacuum at, or close to, the surface ejected droplets of brine crystallize to form ice and carbonate particles. These particles are deposited by fallback and form the observed surfaces once the ice component has sublimated.

Here we combine morphological analyses of Cerealia and Vinalia Faculae observed by Dawn's Framing Camera (FC) (Sierks et al., 2011) with geophysical models to consider these three scenarios and to provide insights on the material composition, independent of the observations by the Dawn near-infrared spectrometer. Morphological analyses are strengthened by a topographic map calculated from FC stereo imaging. The geophysical models considered here follow previous studies on mound (cones and domes) formation (Brož et al., 2014; Quick et al., 2016), ice sublimation (Landis et al., 2017) and particles in a gas stream (Schmidt et al., 2008).

2. Observations

Geomorphological analyses are performed with radiometrically calibrated FC images and stereo-photogrammetric Digital Terrain Model (DTM). FC images have a spatial resolution of ∼35 m/pixel and the DTM has an image scale of ∼32 m/pixel (1.5-m-vertical accuracy) (Jaumann et al., 2017; Preusker et al., 2015). The unique photometric properties of the faculae prevent a reliable albedo retrieval at this stage and thus a definition of bright material based on this optical characteristic (e.g., Schroeder et al., 2017). Therefore, we define the bright faculae to be material with reflectance 2-σ above the mean reflectance of a 40-km-wide box area centered on Vinalia Faculae. This approach is used on a single FC observation (FC59290), with incidence angle 48°, emission angle 4°, and phase angle 47°, containing both Vinalia and Cerealia Faculae. More than a dozen isolated areas of bright material are detected on the floor of Occator crater (Fig. 1), often exhibiting a mantle morphology. We restrict the morphological analyses to the largest three sites. The morphological mapping process was supported by inspection of additional FC images of different observation geometries.

2.1. Vinalia Faculae

The first two sites belong to Vinalia Faculae. Site 1 has an approximately circular 5-km-diameter bright mantling crossed by a system of 100-m wide fractures (Buczkowski et al., 2018). At the center, a 500-m-wide polygonal structure is present (Fig. 2a). The sides of the structure appear darker, and resemble in brightness and width, the nearby fractures. The resemblance of the darker sides to the walls of a pit or of an impact crater suggests that the central structure is a potential depression, although it is not identifiable on the DTM. The pattern of bright mantling varies as a function of the distance from the central structure. Close to the center the mantling is widespread. At the edges, instead, the material is scattered in patches (Fig. 2c and d). The reason for such scattered contact with the surrounding terrain might in part be due to the roughness ("ropy") nature of the terrain (Fig. 2c and d) (Scully et al., 2018; Nathues et al., 2018) influencing the deposition of the material. We note that there is no evidence for flowing, such as flow fronts. At this location the thickness of the bright material has been estimated from several meters up to a few tens of meters (Nathues et al., 2018). An impact origin for the rimless central structure and the surrounding mantling can be excluded because of the absence of a bowl-shaped interior and the mantling diameter relative to the depression diameter, exceeding
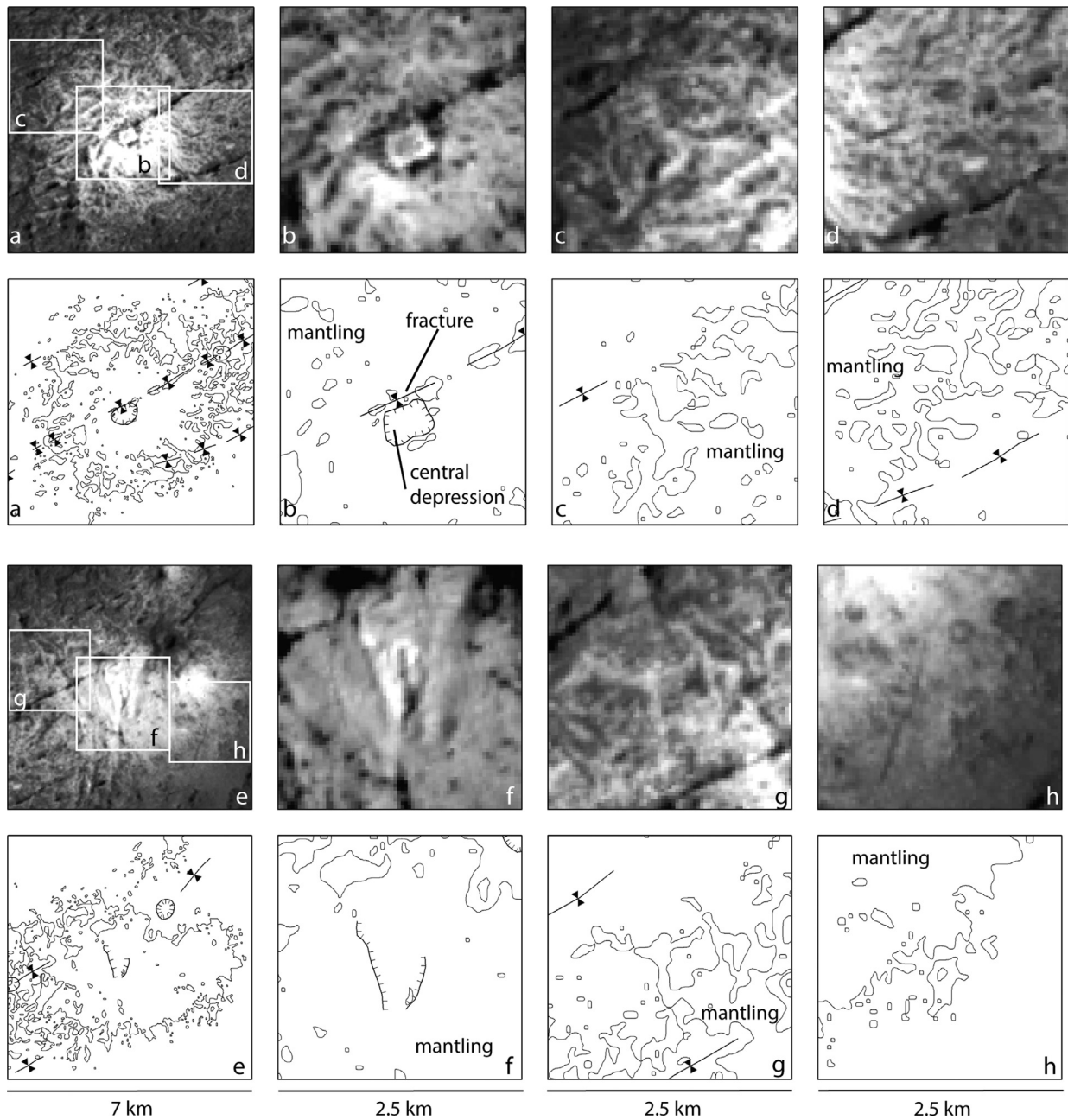
Fig. 2. FC 59290 close-ups of Site 1 (a, b, c, d) and Site 2 (e, f, g, h). Below each close-up is an associated diagram where the spatial contour of the bright material is shown and key morphologies are highlighted. Note that both Site 1 and Site 2 have continuous bright material close to the center and patchy distribution at the edges. Line with mirrored black arrows indicates a fracture, whereas line with inward ticks indicates a possible depression. See text for the definition of the bright material. Illumination direction is from the right.

that of a simple crater's ejecta blanket (Melosh, 1989). Nevertheless, the central structure, appearing as a subtle depression, surrounded by mantling fading with distance from the center is reminiscent of local, violent disruption of the upper surface and ejection and fallback deposition of material.

Site 2 shows comparable morphologies. The mantling has an extent of approximately 5-km, crossed by the same system of fractures as Site 1. The central structure consists of two ridges in a V-shaped configuration creating an irregular depression (Fig. 2e and f) (Fig. 5 in Nathues et al., 2018). As at Site 1, bright material is widespread and continuous at the center (Fig. 2f) and discontinuous at the edges of the facula (Fig. 2g and h). The central structure and mantling are again indicative of surface disruption and material ejection, and are not consistent with impact cratering.

2.2. Cerealia Facula

Cerealia Facula, referred here as Site 3, presents similar morphologies as the previous sites with the addition of a central dome, 3-km-wide and about 400-m-high (Fig. 3a–c). The dome is dissected by a system of radial fractures up to 200-m-wide with juxtaposed depressions up to ~300 m wide (Fig. 3b, central panel). The depressions' irregular shapes, lack of rims, and association with fractures argue against an impact cratering process. South of the dome, the transition between the dome and the surrounding smooth area is identifiable only in the topography, i.e., there is no change in surface brightness or texture between the bright material of the dome and of the adjacent area (Fig. 3d). This lack of morphological contact indicates that the dome formed by uplift-
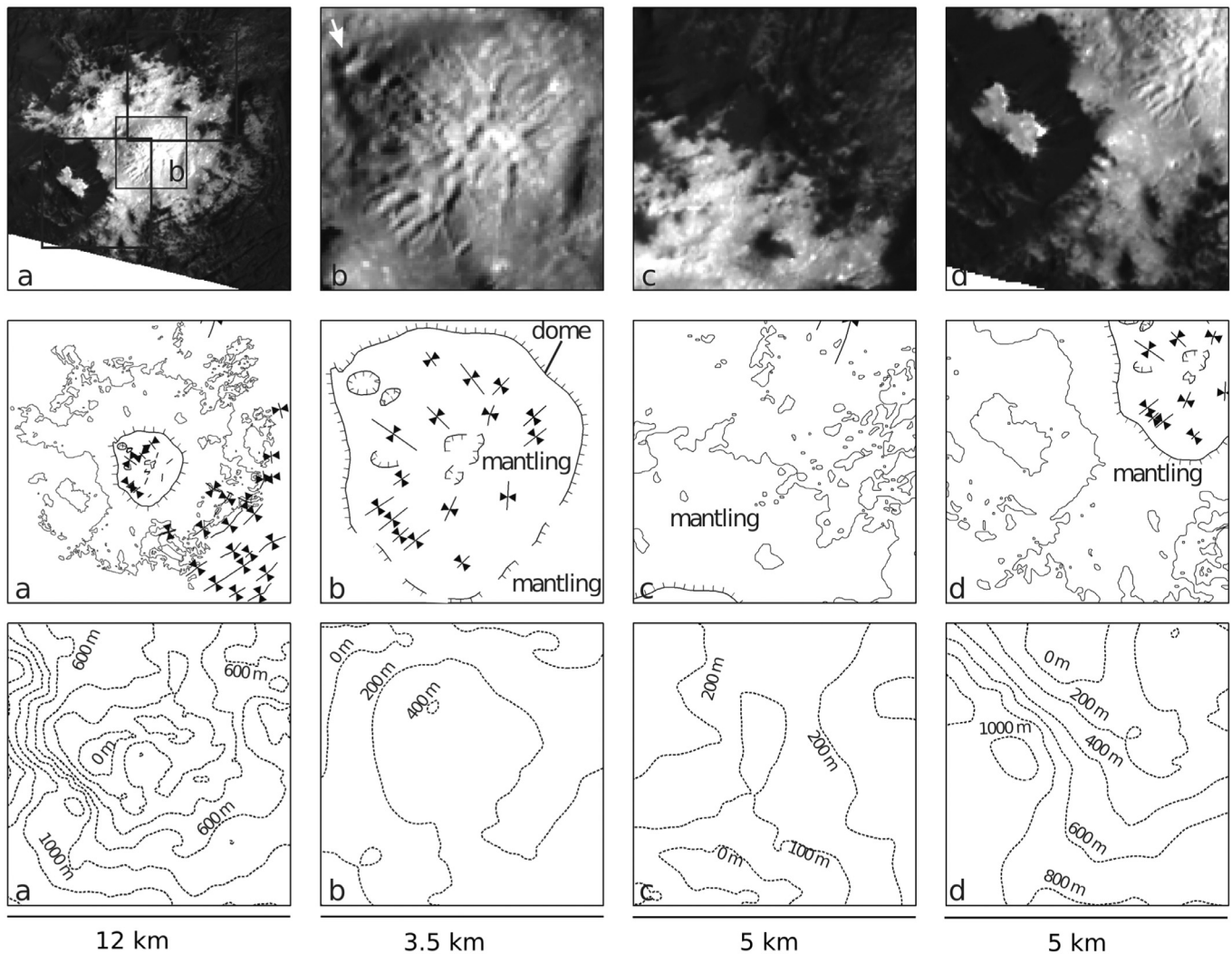
Fig. 3. Upper row: FC 59290 close-ups of Site 3. Illumination direction is from the right. Middle row: associated diagram for each close-up where the contour of bright material and key morphologies are shown. Line with outward ticks indicates a topographic dome. Lower row: associated diagram for each close-up showing contour lines of elevation each 200 m. For clarity, the deepest point is arbitrarily taken as zero elevation.

ing of a brittle layer or that deposition of a thin bright mantling occurred after the dome was emplaced. To the northwest of the dome, the potential embayment of a dome depression by the surrounding material suggests flowing of bright material after dome formation (arrow in Fig. 3b upper panel). A single formation process for the dome cannot be determined based on these morphological relationships; instead, a set of processes may have co-occurred, including uplifting, mantling, and flowing. In contrast to the ropy and low topographic relief of the underlying surfaces (below the mantling) of Site 1 and 2, Site 3 is found within a 500–1000 m deep central pit (Krohn et al., 2016; Nathues et al., 2017b; Scully et al., 2018). Different relationships between this topographic context and the distribution of bright mantling at Site 3 are observed. In one location (Fig. 3c, lower panel) there are no embayment morphologies, i.e., the pattern of the bright material does not follow the topography. In another area, at the edge of the facula, the pattern of the bright material follows topographic contours (Fig. 3d lower panel) with a remarkably sharp transition (Fig. 3d upper panel). This embayment relationship can be a product of mass wasting, i.e., covering of bright material by darker material in steep sloped terrains, creating apparent topographic control on the original bright material distribution. Evidence for a for-

merly more extensive distribution of bright material and subsequent darker covering or erosion by mass wasting is shown in Fig. 3d, where a topographic peak (part of the rim of Occator central pit) is covered by an isolated 1.4-km long bright patch, surrounded by steep-sided darker material with a sharp contact. We measure a 1-km topographic step between the bright topographic peak and the center of the facula (Fig. 3d lower panel). The rim of Occator central pit and the associated peak were already present at the time of faculae formation (Nathues et al., 2017b). This suggests an emplacement of bright material by deposition from fallback and disfavor upslope flowing from the center of the faculae toward the edges and up to the peak.

The mantling pattern changes with distance from the center, with patchy distributions found at the edges of the facula in the absence of a ropy surface (Fig. 3c and d). This pattern indicates that scattered patches are not only the result of the underlying topography (e.g., ropy surface of Site 1) and can be the consequence of the formation and/or post-formation processes of the faculae. Formation of scattered patches could be the result of ejection and fallback of material, whereas post-formation processes could include erosion by sublimation of ice-rich material and thermal segregation of ice into patches (Spencer, 1987). Both radial and circumfer-

ential fractures approximately 200 m in width cross the mantling, similar to what is seen in Sites 1 and 2. The crossing of darker fractures into the brighter mantling suggests that fracturing continued, or started, after the mantling emplacement.

3. Models and discussions

The distribution of the mantling has its characteristic continuous-to-patchy property repeatedly observed in all three sites, with large (~1-km) bright patches scattered non-uniformly at great distances from the center. These shared morphologies suggest related formation processes, and strongly suggest a single transporting material, supported by anhydrous sodium carbonate consistently detected at the three sites (DeSanctis et al., 2016). In addition, the transport mechanism was able to disrupt the surface, as the central structures at Vinalia Faculae suggest, and create a dome (by uplifting, mantling and/or flowing), as the morphologies at Cerealia dome indicate. We consider the three possible formation mechanisms of ice ascent, gas emission, and brine extrusion.

3.1. Ice ascent

In this scenario, a region of water ice mixed with carbonate is found a few to several tens of km deep in the subsurface. Ascent of this ice is facilitated by crustal fracturing of Occator impact. The density and viscosity of this ice, a function of the abundance of high-density particles, must be such to enable ascent by buoyancy in Ceres low density crust. The central structures represent the location where the ice reaches the surface. Note that in this scenario a cometary analog to the central structures could be pits (e.g., Vincent et al., 2015; Mousis et al., 2015). Once exposed at the surface, ice bearing carbonate particles is subject to sublimation. During sublimation, the carbonate particles are lofted and fallback to the surface to form a mantle. Lofting and fallback are probably a quasi-stationary process that would lead to a continuous mantling with radially sorted particle size, rather than the observed highly variable scattered distribution, suggesting violent, perhaps non-steady events. We note that lofting of particles by ice sublimation should satisfy the requirement to lift the particles from the center of the facula up to the 1-km high topographic peak (Fig. 3d). The maximum size of the particles that can be lofted is set by the maximum daytime temperature of ice (albedo dependent) and the ice area (solid angle seen by the particle) (Landis et al., 2017). Landis et al. (2017) find that even a 5-km radius circular ice patch at 180 K does not loft > 10 μm particles higher than 1-km above the surface. This particle size is lower than that estimated with near-infrared spectral observations (De Sanctis et al., 2016). Absorption bands detected with reflectance spectroscopy are produced by particle scattering in the geometric-optics region where particle size is much larger than the radiation wavelength (e.g., Hapke, 2012). In fact, radiative transfer modeling of sodium carbonate absorption bands at Cerealia Facula estimated the carbonate grain size at $71 \pm 14 \, \mu m$ (De Sanctis et al., 2016). In addition, here we are not considering the lateral distribution of particles. Lofting should not only raise particles up to 1-km high but also spread them horizontally for several km to form the observed mantling around the central structure.

3.2. Gas from clathrate decomposition

In this scenario, ejection of carbonate particles up to the surface is driven by an ascending gas released by clathrate decomposition. The fallback of these particles forms the mantling. Here we do not investigate the ejection of these particles (a similar case

is considered for the brine scenario in the next section) and directly study the formation of the Cerealia dome by fallback accumulation. Continuous fallback deposition of particles ejected by the vent is expected to form topographic relief analogous to a scoria cone (e.g., Bemis and Ferencz, 2017). The cone formed by particle fallback will be composed of unconsolidated debris and may be subject to downslope mass wasting if the value of static angle of repose is exceeded. Morphologies supporting such processes on Ceres include debris avalanches, as observed on the talus area of Ahuna Mons (Ruesch et al., 2016). The north-facing slopes of the Cerealia dome are ~40° steep but without striations, indicating no downslope avalanches of debris. Instead, fractures and depressions are observed indicating the flanks are dominated by cohesive material with minor coverage by debris.

To study this scenario further, we evaluate whether the same particles ejected to form the mantle can also accumulate near the vent to form a debris cone, and whether the cone dimensions match those of the dome in Site 3 (Fig. 3b). We assume that the mantling of Site 3 is formed similarly as the other sites, i.e., by particles ejected over a wide range of ejection angles. Such broad ejection angles are justified by the presence of central structure, which plays the role of a flared-shaped vent. This vent geometry broadens the angles of the collimated stream ascending the conduit (e.g., Wilson and Head, 1981; Kieffer, 1984). Thus, with an ejection angle of 45° (Table 1), the radius of the Site 3 mantling defines the ejection velocity of the particles at ~37 m s^{-1} ($v = \mathrm{sqrt}(r{*}g)$, where r is the mantling radius and g is Ceres gravity, Table 1). The shape of a putative debris cone can be reconstructed by taking into account this ejection velocity of the particles, the distribution of the angles of ejection, Ceres's gravity (Brož et al., 2014), and assuming that the angle of repose is independent of the gravity (e.g., Atwood-Stone and McEwen, 2013; Ewing et al., 2017). For the particle ejection angles we consider a Gaussian distribution, as successfully used in previous scoria cone modeling (Brož et al., 2015). We find that with a half width of 45° from the vertical, an extremely broad cone develops that does not match the aspect ratio of the dome of Site 3 (Fig. 4, with ~37 m s^{-1} approximated at 40 m s^{-1}). To reproduce the dome's aspect ratio the particle ejection angles need to be extremely narrow, with a half width only 2.5° from the vertical (Fig. 4). These narrow ejection angles are at odds with the broader angle distribution suggested by the vent geometry. Considering higher ejection velocity will require even more extreme small angles (≪2.5°) to form the cone and thus extremely focused jets. Assuming the same process has formed the cone and the bright mantle, the formation of the Site 3 features by the same fall back material seems unlikely. However, from this modeling alone, it cannot be excluded that the dome and bright mantle have formed as results of two different ejection processes with a narrower and wider ejection angle, respectively. In the next section, we investigate a more complex formation scenario involving a briny liquid.

3.3. Brine ascent

Upon brine ascent and decompression in a conduit, the brine will be subject to evaporation and flash freezing will form carbonate and ice grains (e.g., Postberg et al., 2009; Zolotov, 2017; Vu et al., 2017). Evaporation as well as fragmentation (discussed below) is a violent stage (high vapor speed) that could be responsible for surface disruption and formation of the central structures. The ejection and fallback of the particles can form the mantling if they are ejected ballistically at sufficient speed. Here we evaluate the two main factors controlling the ejection speed (temperature of the gas and conduit width) and compare the plausible ejection speeds with those required to form the observed bright mantling. We use the gas-kinetic theory and the equation of motion of par-

Table 1
Summary of key parameters used in Sections 3.2 and 3.3.

| Parameter	Value	Reference
Diameter of bright mantle for Sites 1 and 2	5 km (measurement)	Fig. 2
Diameter of bright mantle for Site 3	10 km (measurement)	Fig. 3
Maximum conduit width (Sites 1, 2)	500 m (hypothesis)	Fig. 2
Ejection speed of particles for Sites 1 and 2	26 m s^{-1} (calculated)	Fig. 2
Ejection speed of particles for Site 3	37 m s^{-1} (calculated)	Fig. 3
Particle radius (R)	$7.1 \pm 1.4 \times 10^{-5}$ m (literature)	De Sanctis et al. (2016)
Gas velocity (u_{gas})	500 m s^{-1} (hypothesis)	
Density of anhydrous sodium carbonate particle (ρ_{grain})	2540 kg m^{-3} (literature)	
Mass of water molecule (m_0)	2.99×10^{-26} kg (literature)	
Boltzmann constant (k_B)	1.38×10^{-23} J K^{-1} (literature)	
Ceres gravity (g)	0.28 m s^{-2} (literature)	Russell et al. (2016)
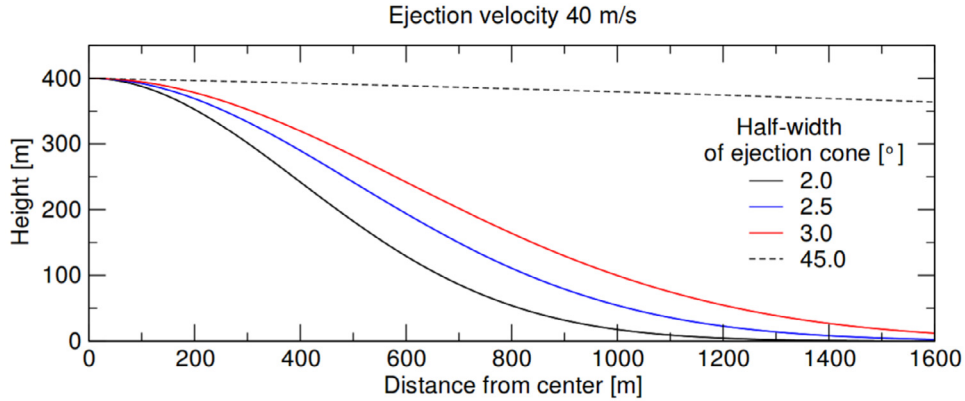
Fig. 4. Simulated half topographic profiles of a cone formed by accumulation of fallback particles, ejected with different half-widths of ejection cone, at a velocity of 40 m s^{-1}. Angles of 2.0°, 2.5° and 3.0° approximate the dimensions (400 m high, 1.5 km radius) of the Cerealia dome (Site 3, Fig. 3b). For comparison, a profile for a 45° half-width of ejection cone is shown.
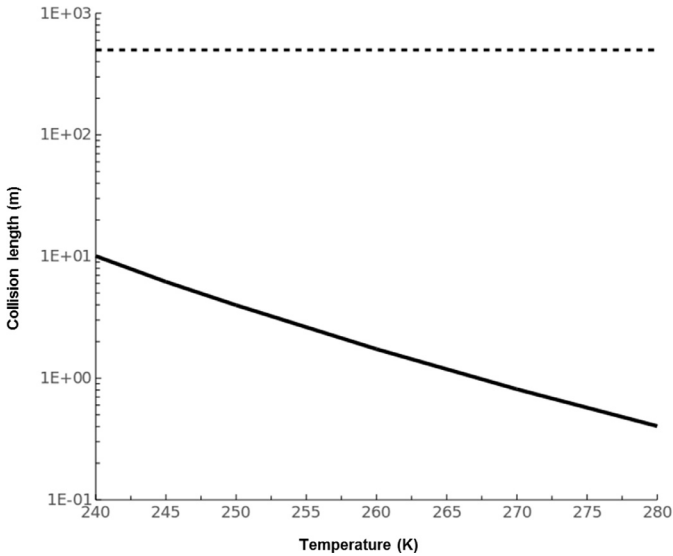

Fig. 5. Minimum collision length necessary for a raising water vapor of given temperature to accelerate carbonate particles up to 26 m s^{-1}, and thus form a halo of the dimensions of Sites 1 and 2. Dashed line is the maximum conduit width inferred from the central structures of Sites 1 and 2.

ticles in a gas stream (e.g., Crowe et al., 2012) as in a model developed in Schmidt et al. (2008) and Brilliantov et al. (2007), and similarly to Degruyter and Manga (2011). For simplicity we consider that particles are pure carbonate grains only, whereas they might be composed of both carbonate and ice, and might grow during ascent by condensation and absorption of water molecules. Carbonate particles of density ρ_{grain} and radius R (Table 1) are accelerated by water vapor (from brine evaporation) of speed u_{gas} and density ρ_{gas} (both a function of temperature) in a conduit of given width. The width of the conduit, much smaller than the conduit length, is critical because particles velocity is reduced to zero in a collision with the conduit walls (Schmidt et al., 2008). Thus, the conduit width roughly determines the collision length (L), which can be described as (Brilliantov et al., 2008):

$$L = \frac{R}{2\omega\rho_{gas}(T)\sqrt{T}(\langle u_{grain}\rangle^{-1} - u_{gas}^{-1})} \quad (1)$$

with $\langle u_{grain}\rangle$ the average velocity of particles and the coefficient ω defined as:

$$\omega = \frac{\langle w_{gas}\rangle}{\rho_{grain}\sqrt{T}}\left[1 + \frac{\pi}{8}(1 - \beta)\right] \quad (2)$$

Parameter β describes the condensation and absorption of gas molecules by the growing grains. In this simple case the particles are considered to be pure carbonate and therefore not subject to growth ($\beta = 0$). Parameter $\langle w_{gas}\rangle$ is the average molecular speed of the gas at temperature T, or:

$$\langle w_{gas}\rangle = \sqrt{\frac{8k_B T}{\pi m_0}} \quad (3)$$

With k_B the Boltzmann constant and m_0 the water molecule mass (Table 1). We define the velocity of the water vapor u_{gas} with its thermal velocity at 270 K, i.e., 500 m s^{-1}. The density is that of saturated water vapor, considered a perfect gas at the liquid-vapor equilibrium (S27 in Schmidt et al., 2008). Particle size (R) and density (ρ_{grain}) are set to the carbonate grain size (71 ± 14 µm) and density (2540 kg m^{-3}) determined with near-infrared observation (De Sanctis et al., 2016). Here we take the example of Vinalia Faculae, where mantling (putative fallback deposits) and central
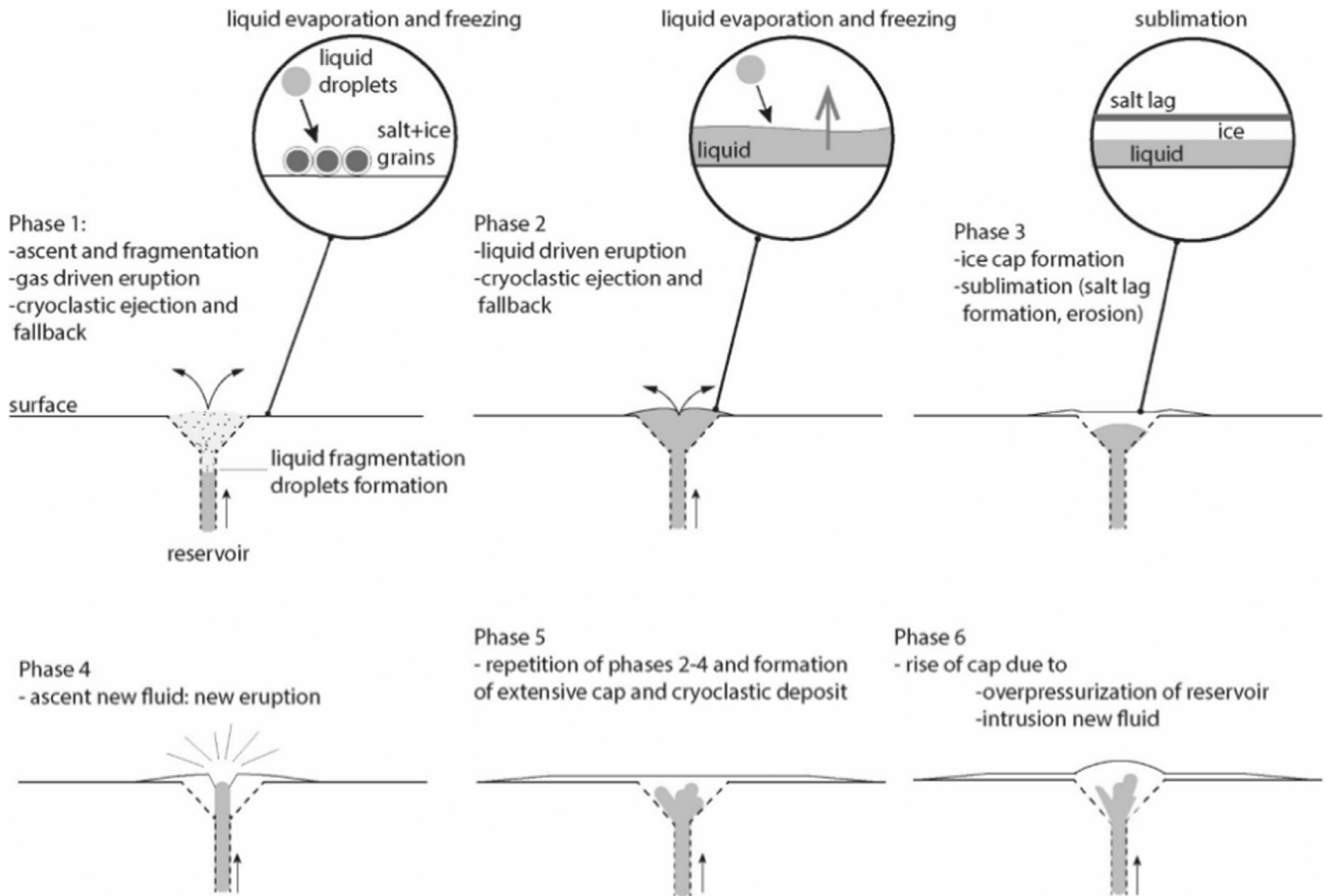
Fig. 6. Schemes illustrating the different phases during brine extrusion. Phase 1 is characterized by brine evaporation, fragmentation and extrusion of water vapor entraining flash freezed particles of salt and ice. Phases 2–5 show extrusion of high viscosity brine with subsequent freezing and sublimation. Phase 6 illustrates dome formation.

structures (putative vents) are well expressed. By taking into account the average 2.5-km radius of the mantling, the required particle speed is 26 m s^{-1} ($\langle u_{grain} \rangle$ in Eq. (1)), if we assume an ejection angle of 45°. The use of this ejection angle is again justified by the presence of the central structure (e.g., Kieffer, 1984; Glaze and Baloga, 2000). An upper estimate for the conduit width is the measured size of the central structure of Site 1, 500 m. While this value is used here, we consider that plausible conduit width is in the range 1–100 m, because vents are larger than the underlying feeding conduits (Wilson and Head 1981, 2017) and because large conduits might not be structurally possible (Miyamoto et al., 2005; Quick and Marsh, 2016).

We find that temperatures of about 270 K are required for collision length of ∼1 m (Fig. 5). Although this minimum temperature is consistent with a liquid brine, it is higher than the modeled crustal temperatures at several tens of km depth. For a temperature of 245 K, more consistent with those expected at depth and at which a brine might still be liquid (e.g., Castillo-Rogez et al., submitted), the minimum collision length is 6 m, a value within the range inferred for the conduit width. In these conditions, a bright mantling could form without the need for the briny liquid to reach the surface (Fig. 6, phase 1). This result also supports a similar scenario proposed in Zolotov (2017). We note that in addition to evaporation and flash freezing during ascent, the brine can be subject to fragmentation. This can occur by nucleation and expansion of gas bubbles (e.g., CO$_2$), resulting in the disruption of the brine into a gas phase and a spray of liquid droplets (e.g., Wilson et al., 2010; Zolotov, 2017). Due to Ceres' low gravity, this effect will be

important even if dissolved gases are present in low concentration (<1 wt.%) (Fagents et al., 2000; Quick, 2018). Whether the briny liquid reaches the surface after these initial phases (evaporation, freezing, fragmentation) will be considered next for the case of the Cerealia dome.

It is conceivable that after the initial stage of eruption dominated by evaporation, gas exsolution and brine disruption in the conduit (Fig. 6, phase 1), brine viscosity will increase by growth of salt crystals and gas content will be lost during ascent. These changes will minimize bubble growth and will decrease the disruption depth. Eventually the brine will reach the surface without being disrupted, and will be subject to boiling at the surface (Fig. 6, phase 2). There, boiling will continue until a carapace of ice is formed (Fig. 6, phase 3). According to Quick (2018) approximately 227 days are needed to form a 1.3 m thick carapace. At which point the pressure below the carapace will compensate the vapor pressure of the brine assuming 25 wt.% of dissolved salts in the brine. This process of carapace formation is probably nonsteady, because during its development and before the required thickness is reached, it will undergo repeated disruption, ejecting blocks <1.3 m across (Fig. 6, phases 4 and 5) (Fagents, 2003). In this scenario, we might expect a non-uniform and scattered distribution of material (Fig. 3).

In addition to the carapace formation, a domical landform could develop by the following processes (Fig. 6, phase 6): (i) bulging of the carapace and/or (ii) extrusion of high-viscosity brine and dome build-up with intrusion. For case (i), bulging could occur by over-pressurization of a freezing subsurface reservoir (e.g.,

Fagents, 2003; Manga and Wang, 2007; Michaut and Manga, 2014) or by an advancing freezing front in a subsurface ice lens. The latter effect would play a role if an inter-connected liquid brine existed at Cerealia and Vinalia Faculae (different in elevation and with a theoretical hydrostatic difference), in analogy to a pingo formation process (e.g., Dundas and McEwen, 2010; Burr et al., 2009). In case (ii) the brine must have a high viscosity, otherwise flooding will occur without topographic built-up. We adopted the gravity current model developed in Quick et al. (2016) to estimate the viscosity required to form a dome with the dimension of Cerealia (Site 3). The model assumes extrusive dome formation, where domes are emplaced by the eruption and subsequent relaxation of viscous material at the surface. According to Quick (2018), plausible emplacement times for the Cerealia dome are between 2.5 and 273 days, assuming bulk kinematic viscosities between 10^6 and 10^8 m^2 s^{-1} at the onset of relaxation to form the dome. These viscosity values include the viscosity of the solid, outer carapace. Thus, brine viscosities at the time of eruption may be as low as 10^2–10^5 m^2 s^{-1}, or 10^5–10^8 Pa s (Quick, 2018; Quick et al., 2016, 2017). This indicates that the initial viscosity of the brine before extrusion (<1 Pa s) must increase by several orders of magnitude. A process responsible for this change can be the precipitation of salt during cooling. Future experimental studies could help in quantifying the effects of this variation. We note that endogenous growth is probably also involved during dome build-up. This process is observed in highly viscous domes and consists of intrusions within the dome with limited flow breaching off the carapace (e.g., Blake, 1990; Annen et al., 2001; Ruesch et al., 2016).

After mantling and dome formation, the near-vacuum conditions will quickly (<1 year) dehydrate any hydrous salts formed by flash freezing of the brine and will leave an anhydrous salt-rich surface layer (Bu et al., 2017), which explains the detection of anhydrous sodium carbonate by near-infrared spectroscopy (De Sanctis et al., 2016). The non-detection of ice at the faculae (De Sanctis et al., 2016) is probably due to sublimation. To quantify the amount of ice retreat due to sublimation (e.g., Titus, 2015; Formisano et al., 2016; Schorghofer et al., 2016), we adopt the model presented in Landis et al. (2017) that considers diurnal temperatures at Occator and water vapor diffusion through a regolith/salt-bearing ice. For the latitudes of interest, we find that ice will retreat not more than 1.5 m in 20 Ma, creating a sublimation lag of salts. The presence of remnant ice below a sublimation and dehydration lag at the Vinalia and Cerealia Faculae is thus consistent with the possibility of current sublimation. It remains to be determined, however, whether sublimation can explain the putative haze observations (Nathues et al., 2015; Thangjam et al., 2016). As mentioned above, according to Landis et al. (2017) lofting is only possible for very small particle sizes and for very low elevations.

If the dome is ice-rich, extensional fracturing (Fig. 3b, central panel) due to freezing ice and viscous deformation may be important in its evolution. We adopted the numerical model of Sori et al. (2017), used to study viscous relaxation of Cerean landforms, and found flow velocities of only ~2 m/Myr. Since the estimated age of the dome is several millions years (Nathues et al., 2017b; Neesemann et al., 2018), relaxation has not yet been important in controlling dome morphology. Observed slope asymmetries (Fig. 3b, lower panel) may result from topography preceding dome formation.

4. Conclusions

Using FC observations at the three sites of Cerealia and Vinalia Faculae, we identify similar bright mantling morphologies that are not found elsewhere on Ceres. These locations also have similar sodium carbonate absorption bands detected by near-infrared spectroscopy. Close proximity, and shared morphological and com-

positional properties imply similar mechanisms for their formation involving a common transport material. The various morphologies and morphometries are best explained by a transport material consisting of liquid brine, reaching the surface at high velocity, as in a salt-water fountain. Velocity of the extrusion is first provided by the density-driven pressure gradient and subsequently by the water vapor thermal velocity. The bright mantling of the faculae is explained by brine flash-freezing and grain fallback. Increasing precipitation of salts during cooling can lead to an increase in the brine viscosity and could explain the dome formation at Cerealia Facula. These proposed changes in brine properties during ascent might be modeled and quantified with the support of future experimental measurements. Ice ascent, followed by sublimation and particle lofting, is a less favored scenario as it cannot fully satisfy the constraints from the mantling morphologies. Gas from clathrate decomposition is a less likely scenario as it can be excluded for the formation of Cerealia dome. The age of Cerealia Facula determined with measurements of superimposed small impact craters is several millions years old (Nathues et al., 2017b; Neesemann et al., 2018). Our results imply that this age represents the time of the presence and surface extrusion of salt bearing water, later than the Occator impact event. Also, since Dawn did not observe active water plumes on Ceres (Nathues et al., 2015), such activity must occur on timescales greater than years. Ceres geochemical and thermal evolution must have been able to provide conditions such that frozen brine in the subsurface melted with the heat released by the Occator impact and/or brine was preserved in its liquid phase before the impact event, or even throughout Ceres history, at least in regional-scale subsurface networks or reservoirs. In light of these results, Vinalia and Cerealia Faculae, as well as other bright carbonate surfaces, such as Ahuna Mons, are sites where the chemistry of briny liquid can be investigated. Such studies will shed light into the prebiotic environments hosted by Ceres (De Sanctis et al., 2017).

References

Annen, C., Lenat, J.-F., Provost, A., et al., 2001. The long-term growth of volcanic edifices: numerical modelling of the role of dyke intrusion and lava-flow emplacement. J. Volcanol. Geotherm. Res. 105, 263–289.

Atwood-Stone, C., McEwen, A.S., 2013. Avalanche slope angles in low-gravity environments from active Martian sand dunes. Geophys. Res. Lett. 40 (12), 2929–2934. doi:10.1002/grl.50586.

Bemis, K.G., Ferencz, M., 2017. Morphometric analysis of scoria cones: the potential for inferring process from shape. Geol. Soc. London Spec. Publ. 446, 61–100.

Blake, S., 1990. Viscoplastic models of lava domes. In: Fink, J.H. (Ed.), Lava Flows and Domes. Springer, pp. 88–126.

Bland, M.T., Raymond, C.A., Schenk, P.M., Fu, R.R., Kneissl, T., Pasckert, J.H., Hiesinger, H., et al., 2016. Composition and structure of the shallow subsurface of Ceres revealed by crater morphology. Nat. Geosci. 9, 538–542. doi:10.1038/ngeo2743.

Brilliantov, N.V., Schmidt, J., Spahn, F., 2007. Nucleation and growth of a solid phase in a gas expanding into vacuum. Int. J. Mod. Phys. C 18 (4), 676–684.

Brilliantov, N.V., Schmidt, K., Spahn, F., 2008. Geysers of Enceladus: quantitative analysis of qualitative models. Planet. Space Sci. 56, 1596–1606. doi:10.1016/j.pss.2008.06.007.

Broz, P., Cadek, O., Hauber, E., Rossi, A.P., 2014. Shape of scoria cones on Mars: insights from numerical modeling of ballistic pathways. Earth Planet. Sci. Lett. 406, 14–23. doi:10.1016/j.epsl.2014.09.002.

Broz, P., Cadek, O., Hauber, E., Rossi, A.P., 2015. Scoria cones on Mars: detailed investigation of morphometry based on high-resolution digital elevation models. J. Geophys. Res. 120, 1512–1527. doi:10.1002/2015JE004873.

Bu, C., Rodriguez Lopez, G., Dukes, C.A., Ruesch, O., McFadden, L.A., Li, J.-Y., 2017. Search for sulfates on the surface of Ceres. Meteoritics Planet. Sci. 1–15. doi:10.1111/maps.13024.

Buczkowski, D.L., Scully, J.E.C., Quick, L., Castillo-Rogez, J., Schenk, P.M., Park, R., Preusker, F., Jaumann, R., Raymong, C.A., Rusell, C.T., 2018. Tectonic analysis of fracturing associated with Occator crater. Icarus in review.

Burr, D.M., Tanaka, K.L., Yoshikawa, K., 2009. Pingos on Earth and Mars. Planet. Space Sci. 57, 541–555. doi:10.1016/j.pss.2008.11.003.

Castillo-Rogez, J.C., McCord, T.B., 2010. Ceres' evolution and present state constrained by shape data. Icarus 205, 443–459. doi:10.1016/j.icarus.2009.04.008.

Castillo-Rogez J.C., et al., Insights into Ceres' evolution from surface composition, Meteoritics Planet. Sci. submitted.

Combe, J.-P., McCord, T.B., Tosi, F., Ammannito, E., Carrozzo, F.G., De Sanctis, M.C., Raponi, A., Byrne, S., et al., 2016. Detection of local H$_2$O exposed at the surface of Ceres. Science 353, 6303. doi:10.1126/science.aaf3010.

Crowe, C.T., Schwarzkopf, J.D., Sommerfeld, M., Tsuji, Y., 2012. Multiphase Flows With Droplets and Particles. CRC Press Taylor and Francis Group.

Degruyter, W., Manga, M., 2011. Cryoclastic origin of particles on the surface of Enceladus. Geophys. Res. Lett. 38, L16201. doi:10.1029/2011GL048235.

De Sanctis, M.C., et al., 2016. Bright carbonate deposits as evidence of aqueous alteration on (1) Ceres. Nature 536, 54–57. doi:10.1038/nature18290.

De Sanctis, M.C., Ammannito, E., McSween, H.Y., Raponi, A., Marchi, S., Capaciconi, F., Capria, M.T., 2017. Localized aliphatic organic material on the surface of Ceres. Science 355, 719–722. doi:10.1126/science.aaj2305.

Dundas, C.M., McEwen, A.S., 2010. An assessment of evidence for pingos on Mars using HiRISE. Icarus 205, 244–258. doi:10.1016/j.icarus.2009.02.020.

Ermakov, A.E., Fu, R.R., Castillo-Rogez, J.C., Raymond, C.A., Park, R.S., Preusker, F., Russell, C.T., Smith, D.E., Zuber, M.T., 2017. Constraints on Ceres' internal structure and evolution from its shape and gravity measured by the Dawn spacecraft. J. Geophys. Res. doi:10.1002/2017JE005302.

Ewing, R.C., Lapotre, M.G.A., Lewis, K.W., Day, M., Stein, N., Rubin, D.M., Sulliva, R., Banham, S., Lamb, M.P., Bridges, N.T., Gupta, S., Fischer, W.W., 2017. Sedimentary processes of the Bagnold dunes: implications for the eolian rock record of Mars. J. Geophys. Res. doi:10.1002/2017JE005324.

Fagents, S.A., Greeley, R., Sullivan, R.J., Pappalardo, R.T., Prockter, L.M., et al., 2000. Cryomagmatic mechanisms for the formation of Rhadamanthys Linea, triple band margins, and other low-albedo features on Europa. Icarus 144, 54–88. doi:10.1006/icar.1999.6254.

Fagents, S.A., 2003. Considerations for effusive cryovolcanism on Europa: the post-Galileo perspective. J. Geophys. Res. 108 (E12), 2139. doi:10.1029/2003JE002128.

Formisano, M., De Sanctis, M.C., Magni, G., Federico, C., Capria, M.T., 2016. Ceres water regime: surface temperature, water sublimation and transient exo(atmo)sphere. Mon. Not. R. Astron. Soc. 455, 1892–1904. doi:10.1093/mnras/stv2344.

Fu, R.R., Ermakov, A.I., Marchi, S., Castillo-Rogez, J.C., Raymond, C.A., Hager, B.H., Zuber, M.T., Kind, S.D., Bland, M.T. et al. (2017). The interior structure of Ceres as revealed by surface topography. submitted for publication.

Glaze, L.S., Baloga, S.M., 2000. Stochastic-ballistic eruption plumes on Io. J. Geophys. Res. 105 (E7), 17579–17588. doi:10.1029/1999JE001235.

Hapke, B., 2012. Theory of Reflectance and Emittance Spectroscopy, second ed Cambridge University Press.

Jaumann, R., Preusker, F., et al., 2017. Topography and geomorphology of the interior of Occator crater on Ceres. 48th Lunar and Planetary Science Conference, Houston March 2017 abstract #1440.

Kieffer, S.W., 1984. Factors governing the structure of volcanic jets. In: Explosive Volcanism: Inception, Evolution, and Hazards. National Academy Press, pp. 143–157.

Kieffer, S.W., Lu, X., Bethke, C.M., Spencer, J.R., Marshak, S., Navrotsky, A., 2006. A clathrate reservoir hypothesis for Enceladus' south polar plume. Science 314, 5806. doi:10.1126/science.1133519.

Krohn, K., Jaumann, R., Stephan, K., Otto, K.A., Schmedemann, N., Wagner, R.J., Matz, K.-D., Tosi, F., Zambon, F., et al., 2016. Cryogenic flow features on Ceres: implications for crater-related cryovolcanism. Geophys. Res. Lett. doi:10.1002/2016GL070370.

Landis, M.E., Byrne, S., Schoerghofer, N., Schmidt, B.E., Hayne, P.O., et al., 2017. Conditions for sublimating water ice to supply Ceres' exosphere. Geophys. Res. Lett. 122, 1984–1995. doi:10.1002/2017JE005335.

Manga, M., Wang, C.-Y., 2007. Pressurized oceans and the eruption of liquid water on Europa and Enceladus. Geophys. Res. Lett. 34. doi:10.1002/2007GL029297.

Melosh, H.J., 1989. Impact cratering: a geological process. Oxford Monographs on Geology and Geophysics, No. 11. Oxford University Press, New York.

Michaut, C., Manga, M., 2014. Domes, pits, and small chaos on Europa produced by water sills. J. Geophys. Res. 119, 550–573. doi:10.1002/2013JE004558.

Miyamoto, H., Mitri, G., Showman, A.P., Dohm, J.M., 2005. Putative ice flows on Europa: Geometric patterns and relation to topography collectively constrain material properties and effusion rates. Icarus 177, 413–424. doi:10.1016/j.icarus.2005.03.014.

Mousis, O., Guilbert-Lepoutre, A., Brugger, B., Jorda, L., Kargel, J.S., Bouguet, A., Auger, A.-T., Lamy, P., Vernazza, P., Thomas, N., Sierks, H., 2015. Pits formation from volatile outgassing on 67P/Churyumov–Gerasimenko. Astrophys. J. Lett. 814, L5. doi:10.1088/2041-8205/814/1/L5.

Nathues, A., Hoffmann, M., Schaefer, M., Le Corre, L., Reddy, V., Platz, T., Cloutis, E.A., et al., 2015. Sublimation in bright spots on (1) Ceres. Nature 528, 237–240.

Nathues, et al., 2018. Occator crater in color at highest spatial resolution. Icarus doi:10.1016/j.icarus.2017.12.021.

Nathues, A., Platz, T., Hoffmann, M., Thangjam, G., Cloutis, E.A., Applin, D.M., Le Corre, L., Reddy, V., Mengel, K., Preusker, F., Schmidt, B.E., Kallisch, J., Russell, C.T., 2017a. Oxo Crater on (1) Ceres – geologic history and the role of water ice. Astron. J. 154 (3).

Nathues, A., Platz, T., Thangjam, G., Hoffmann, M., Mengel, K., Cloutis, E.A., Le Corre, L., Reddy, V., Kallisch, K., Crown, D.A., 2017b. Evolution of Occator crater on (1) Ceres. Astron. J. 153, 112. doi:10.3847/1538-3881/153/3/112.

Neesemann, A., et al., 2018. The various ages of Occator crater, Ceres. Icarus in press.

Neveu, M., Desch, S., 2015. Geochemistry, thermal evolution, and cryovolcanism on Ceres with a muddy ice mantle. Geophys. Res. Lett. 42, 10,197–10,206. doi:10.1002/2015GL066375.

Postberg, F., Kempf, S., Schmidt, J., Brilliantov, N., Belinsen, A., Abel, B., Buck, U., Srama, R., 2009. Sodium salts in R-ring ice grains from an ocean below the surface of Enceladus. Nature 459. doi:10.1038/nature08046.

Preusker, F., Scholten, F., Matz, K.-D., Roatsch, T., Willner, K., Hviid, S.F., Knollenberg, J., et al., 2015. Shape model, reference system definition, and cartographic mapping standards for comet 67P/Churyumov-Gerasimenko – stereo-photogrammetric analysis of Rosetta/OSIRIS image data. Astron. Astrophys 583, A33.

Prettyman, T.H., Yamashita, N., Toplis, M.J., McSween, H.Y., Schoerghofer, S., Marchi, S., Feldman, W.C., et al., 2017. Extensive water ice within Ceres' aqueously altered regolith: Evidence from nuclear spectroscopy. Science 355, 55–59. doi:10.1126/science.aah6765.

Quick, L.C., Glaze, L.S., Baloga, S.M., Stofan, E.R., 2016. New approaches to inferences for steep-sided domes on Venus. J. Volcanol. Geotherm. Res. 319, 93–105. doi:10.1016/j.jvolgeores.2016.02.028.

Quick, L.C., Marsh, B.D., 2016. Heat transfer of ascending cryomagma on Europa. J. Volcanol. Geotherm. Res. 319, 66–77. doi:10.1016/j.jvolgeores.2016.03.018.

Quick, L.C., Glaze, L.S., Baloga, S.M., 2017. Cryovolcanic emplacement of domes on Europa. Icarus 284, 477–488. doi:10.1016/j.icarus.2016.06.029.

Quick, L.C., 2018. A possible brine reservoir beneath Occator crater: thermal and compositional evolution and the formation of the Vinalia Faculae. Icarus Occator special issue, in press.

Ruesch, O., Platz, T., Schenk, P., McFadden, L.A., Castillo-Rogez, J.C., Quick, L.C., Byrne, S., et al., 2016. Cryovolcanism on Ceres. Science 353 (6306). doi:10.1126/science.aaf4286.

Russell, C.T., Raymond, C.A., Ammannito, E., Buczkowski, D.L., De Sanctis, M.C., Hiesinger, H., Jaumann, R., Konopliv, A.S., McSween, H.Y., Nathues, A., Park, R.S., et al., 2016. Dawn arrives at Ceres: Exploration of a small, volatile-rich world. Science 353 (6303), 1008–1010. doi:10.1126/science.aaf4219.

Schmidt, J., Brilliantov, N., Spahn, F., Kempf, S., 2008. Slow dust in Enceladus' plume from condensation and wall collisions in tiger stripe fractures. Nature 451, 7179. doi:10.1038/nature06491.

Schorghofer, N., Mazarico, E., Platz, T., Preusker, F., Schroeder, S.E., Raymond, C.A., Russell, C.T., 2016. The permanently shadowed regions of dwarf planet Ceres. Geophys. Res. Lett. 43 (13), 6783–6789.

Schroeder, S.E., Mottolo, S., Carsenty, U., Ciarniello, M., Jaumann, R., Li, J.-Y., Longobardo, A., Palmer, E., Pieters, C., Preusker, F., Raymond, C.A., Russell, C.T., 2017. Resolved spectrophotometric properties of the Ceres surface from Dawn Framing Camera images. Icarus 288, 201–225. doi:10.1016/j.icarus.2017.01.026.

Scully, J.E.C., et al., 2018. Ceres' Occator crater and its faculae explored through geologic mapping. Icarus Occator special issue, in press.

Sierks, H., Keller, H.U., Jaumann, R., Michalik, H., Behnke, T., Bubenhagen, F., Buettner, I., et al., 2011. The dawn framing camera. Space Sci. Rev. 163, 263–327.

Sori, M., Byrne, S., Bland, M.T., Bramson, A.M., Ermakov, A., Hamilton, C.W., Otto, K.A., Ruesch, O., Russell, C.T., 2017. The vanishing cryovolcanoes of Ceres. Geophys. Res. Lett. 44 (3), 1243–1250. doi:10.1002/2016GL072319.

Spencer, J.R., 1987. Thermal segregation of water ice on the Galilean satellites. Icarus 69, 297–313. doi:10.1016/0019-1035(87)90107-2.

Thangjam, G., Hoffmann, M., Nathues, A., Li, J.-Y., Platy, T., 2016. Haze at Occator crater on dwarf planet Ceres. Astrophys. J. Lett. 833, 2. doi:10.3847/2041-8213/833/2/L25.

Thomas, N., Davidsson, B., El-Maarry, M.R., Fornasier, S., Giacomini, L., Gracia-Berná, A.G., Hviid, S.F., Ip, W.-H., Jorda, L., Keller, H.U., et al., 2015. Redistribution of particles across the nucleus of comet 67P/Churyumov-Gerasimenko. Astron. Astrophys. 583, A17. doi:10.1051/0004-6361/201526049.

Titus, T.N., 2015. Ceres: Predictions for near-surface water ice stability and implications for plume generating processes. Geophys. Res. Lett. 42 (7), 2130–2136. doi:10.1002/2015GL063240.

Vincent, J.-B., Bodewits, D., Besse, S., Sierks, H., Barbieri, C., Lamy, P., Rodrigo, R., Koschny, D., et al., 2015. Large heterogeneities in comet 67P as revealed by active pits from sinkhole collapse. Nature 523 (7558), 63–66. doi:10.1038/nature14564.

Vu, T.H., Hodyss, R., Johnson, P.V., Choukroun, M., 2017. Preferential formation of sodium salts from frozen sodium-ammonium-chloride-carbonate brines – implications for Ceres' bright spots. Planet. Space Sci. 141, 73–77. doi:10.1016/j.pss.2017.04.014.

Wilson, L., Head, J.W., 1981. Ascent and eruption of basaltic magma on the Earth and Moon. J. Geophys. Res. 86 (B4), 2971–3001.

Wilson, L., Head, J.W., 2017. Generation, ascent and eruption of magma on the Moon: new insights into source depths, magma supply, intrusions and effusive/explosive eruptions (part 1: theory). Icarus 283, 146–175. doi:10.1016/j.icarus.2015.12.039.

Wilson, L., Keil, K., McCoy, T.J., 2010. Pyroclast loss or retention during explosive volcanism on asteroids: influence of asteroid size and gas content of melt. Meteoritics Planet. Sci. 45 (8) 1284–1201 doi:10.1111/j.1945-5100.2010.01085.x.

Zambon, F., Raponi, A., Tosi, F., De Sanctis, M.C., McFadden, L.A., Carrozzo, F.G., Longobardo, A., et al., 2017. Spectral analysis of Ahuna Mons from Dawn mission's visible-infrared spectrometer. Geophys. Res. Lett. 44 (1), 97–104. doi:10.1002/2016GL071303.

Zolotov, M.Y., 2017. Aqueous origins of bright salt deposits on Ceres. Icarus doi:10.1016/j.icarus.2017.06.018.